Tribology International 183 (2023) 108383

Contents lists available at ScienceDirect

Tribology International

journal homepage: www.elsevier.com/locate/triboint

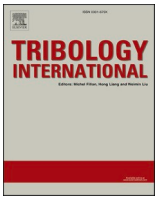

A novel wear-resistant Ni-based superalloy via high Cr-induced subsurface nanotwins and heterogeneous composite glaze layer at elevated temperatures

Fei Liang [a], Ao Meng [a], Yixing Sun [a], Zhaoshuo Chen [a], Zhouwen Jiang [b], Yaping Zhang [a], Yong Zhang [b,*], Yuntian Zhu [c], Xiang Chen [a,*]

[a] Nano and Heterogeneous Materials Center, School of Materials Science and Engineering, Nanjing University of Science and Technology, Nanjing 210094, China
[b] Herbert Gleiter Institute of Nanoscience, School of Materials Science and Engineering, Nanjing University of Science and Technology, Nanjing 210094, China
[c] Department of Materials Science and Engineering, City University of Hong Kong, Hong Kong, China

ARTICLE INFO

Keywords:
Superalloy
Wear resistance
Deformation nanotwins
Composite glaze layer

ABSTRACT

Tribo-induced structural and chemical modifications at elevated temperatures play paramount roles in the tribological performance of Ni-based superalloys. Here, we report on a novel face-centered-cubic Ni-27Cr superalloy with a low stacking fault energy exhibiting remarkable tribological properties at 25–800 ℃, especially the low wear rates at 400 ℃ (1.97×10^{-5} $mm^3/N{\cdot}m$) and 800 ℃ (3.1×10^{-6} $mm^3/N{\cdot}m$). First, at 25–600 ℃, tribo-induced deformation nanotwins show superior structural stability, contributing to the high wear resistance. Second, at 800 ℃, the tribo-induced nanotwins are not formed. Instead, the topmost glaze layer transits from homogeneous nanostructure to heterogeneous microstructure consisting of hard nanograined oxides and soft ultrafine grained matrix. The strong and ductile heterogeneous composite glaze layer accommodates large plastic deformation and reduces wear loss.

1. Introduction

Classical nickel-based superalloys consist of face-centered-cubic (FCC) matrix and strengthening phases, having superior mechanical properties and incredible resistance to creep and oxidation at elevated temperatures [1–7]. They are enabled by solution-strengthening elements (Cr, Mo and W etc.) and/or precipitation-strengthening phases (γ'-Ni_3Nb and γ'-Ni_3(Al, Ti) etc.) [1,3]. Each alloying element normally makes up a concentration less than about 20 at%. Even though Ni-based superalloys are widely applied in aircraft engines and gas turbines industries, their wear resistance limits the service reliability [8–11]. Tribological loading at high temperatures basically leads to the formation of glaze layer consisting of nanostructured oxides which are basically hard but brittle [12–15]. It should be pointed out that the tribo-materials were always under debate in correlating with the tribological properties [16–18]. For example, it has been found that some spinel oxides such as (Ni,Cr)Co_2O_4 and Fe_3O_4 formed during the tribo-oxidation process lead to the reduction of friction coefficient [19,20]. However, some metallic oxides with relatively high melting point such as Al_2O_3 and Mn_2O_3 would act as abrasives to deteriorate wear resistance instead of being sintered into the glaze layer [21]. In other words, the tribo-induced structural and chemical modifications in the superficial layer are decisive for the friction and wear properties of nickel-based superalloys [19,22,23].

In addition to the effect of glaze layer on the friction and wear resistance, rational design of tribo-induced nanocrystalline-amorphous nanocomposite or heterogeneous nanostructure before wear have been successful in suppressing strain localization during the wear process [24]. It was found that the superior wear resistance of $(TiNbZr)_{75}Ag_{25}$ is due to the formation of a strong and deformable nanocomposite surface layer consisting of Ag nanocrystals and TiNbZr-O amorphous oxide during sliding [25]. It was also reported that strain localization in the subsurface region is suppressed by introducing heterogeneous gradient nanostructures in the Cu and Cu-Ag alloy [26,27]. However, tribo-induced nanograins would suffer from grain coarsening and the deterioration of wear resistance [28]. Twin boundaries (TBs) as low-energy planar defects are effective in strengthening metals [29–32]. Not only that, nanotwins were recently verified to be mechanically and thermally stabler than nanograins. It was found that the high hardness and strain hardening ability of nanotwins contribute to the superior

* Corresponding authors.
E-mail addresses: yong@njust.edu.cn (Y. Zhang), xiang.chen@njust.edu.cn (X. Chen).

https://doi.org/10.1016/j.triboint.2023.108383
Received 20 December 2022; Received in revised form 16 February 2023; Accepted 2 March 2023
Available online 3 March 2023

tribological properties of Al-Ni alloys [33]. Taking deformation mechanisms under tribological shear into consideration, it might be an alternative strategy to enhance the high temperature wear resistance of superalloys through introducing tribo-induced high-density of deformation nanotwins into the subsurface region.

In the present study, a new Ni-27Cr-5 W-1Co-1Mo (referred to as Ni-27Cr) superalloy with the relatively low stacking fault energy (SFE) was designed by significantly increasing the Cr content, in an effort to activate tribo-induced twin strengthening (Compared to pure Ni, the reduction of SFE ($\Delta\gamma_{ssf}$) of Ni-27Cr superalloy by the addition of Cr, W, Co and Mo elements into the Ni-based alloys is calculated as 100.6% [34]. It is found that the CM247LC superalloy with a similar $\Delta\gamma_{ssf}$= 105.8% manage to activate twinning behavior during the deformation at 760 ℃ and 870 ℃ [35]. Thus, it is reasonable to verify that our Ni-27Cr superalloy has a low SFE value and tends to activate deformation twinning during the wear process at elevated temperatures). Tribo-induced structural evolutions and chemical changes in the topmost glaze and subsurface layers were studied at different temperatures. In order to reveal the wear-resistant subsurface features, the formation process of heterogeneous composite glaze layer was correlated with tribological data at elevated temperatures.

2. Experimental

2.1. Materials fabrication

The as-cast Ni-27Cr ingots were fabricated by vacuum arc melting in a water-cooled copper crucible under Ar atmosphere. The ingots were flipped and re-melted to insure the homogeneity of chemical composition. The measured alloy composition is listed in Table 1. Specimens for subsequent hardness and tribological testing were cut by electrical discharge machining from the as-cast ingots.

2.2. Hardness and tribological testing

The hardness testing was performed at room temperature on a hardness tester (Shimadzu, HMV-G 21DT, Japan) using a Vickers diamond pyramidal indenter with an applied load of 980.7 mN and a duration time of 10 s. Before the wear test, the surface of Ni-27Cr superalloy was mechanically and electropolished to avoid the effect of surface roughness on the wear properties. Dry sliding wear tests at room and elevated temperatures were conducted on a general tribometer (Bruker, UMT-II, USA) and a high temperature tribometer (Kaihua, GF-I, China), respectively. The counterpart was an Al_3O_2 ball with a diameter of 6.35 mm. The sliding speed and stroke were set as 10 mm/s and 2 mm, respectively. Normal loads of 1, 2, 5 and 10 N were applied in the wear tests at room temperature. The high-temperature wear tests were conducted at 200 ℃, 300 ℃, 400 ℃, 500 ℃, 600 ℃, 700 ℃ and 800 ℃ with a load of 10 N. The total sliding cycles of wear tests are set as 9000 cycles. The coefficient of friction (COF) value (μ) was obtained by $\mu = F/P$, where F is the frictional force measured by the tester and P is the normal applied load. The wear rate is calculated by $k = \frac{V}{S \bullet F_n}$ where V is the wear volume loss measured by a laser scanning confocal microscope (LSCM, OLS4000, Japan), S is the total sliding distance and F_n is the normal load.

2.3. Microstructure characterization

The original microstructure was characterized by a scanning electron microscope (SEM, Zeiss Auriga, Germany) equipped with an electron back-scattered diffraction system (EBSD, Oxford Aztec 2.0, UK) and an Oxford energy dispersive X-ray spectrometer (EDS). The morphology of the wear scars was characterized by a combination of SEM and LSCM. TEM samples were prepared by a focused ion beam (FIB, Zeiss Auriga, Germany) in the middle regions of wear scars. Prior to FIB milling, a Pt layer was deposited on the specific area to protect the worn surface upon exposure to the Ga^+ beam. Then, wear-induced structural and chemical alterations were characterized by a transmission electron microscope (TEM, FEI Titan G2, USA) equipped with an EDS detector (Oxford Instruments Link Isis, UK).

Table 1
The measured element composition of Ni-27Cr superalloy.

Elements	Cr	W	Co	Mo	Ni
at%	27.40	4.55	1.22	1.35	Bal.

3. Results

3.1. Microstructure

The EBSD inverse pole figure (IPF) map in Fig. 1(a) reveals that the original Ni-27Cr superalloy is composed of equiaxed grains with random orientation. The mean grain size is 60 μm, as shown in Fig. 1(b). Some annealing twins could be found within the coarse grains. Fig. 1(c) shows the magnified SEM observation and corresponding EDS mapping within one single grain. Several particles enriched in W and Mo elements could be intermetallic precipitates which may need further investigation.

3.2. Wear properties

Fig. 2(a) shows the COF curves versus the number of cycles at room temperature. When the load varies from 1 N to 5 N, the COF increases immediately upon sliding and tends to approach a steady state at 0.60 after 2500 cycles. The fluctuation degree of COF curve dramatically increases with increasing normal load to 10 N and the average value reaches 0.72, which could be attributed to the formation of massive wear debris during the dry sliding process. Similarly, the wear rate slowly increases with increasing load to 5 N and then increases significantly to 1.4×10^{-4} mm^3/N·m when the load reaches 10 N (Fig. 2(b)). At elevated temperatures, the fluctuation degree and COF value significantly decrease with increasing temperature from 25 ℃ to 400 ℃ (Fig. 2(c)). As the temperature further increases to 800 ℃ (Fig. 2(d)), the COF reduces somewhat to around 0.35, while the wear rate significantly dropped to 10^{-6} order of magnitude. Fig. 3 summarizes the COF and wear rate of the current Ni-27Cr superalloy and other commercial superalloys as a function of applied temperature [8,22,36,37]. The COF and wear rate of the most superalloys decrease with increasing temperature to 800 ℃. At room temperature, the wear rate of our Ni-27 superalloy is comparable to those of Inconel 728/625 superalloys having much higher hardness. At the range of 400–800 ℃, the Ni-27Cr superalloy exhibits superior tribological properties marked as smaller COF and wear rate. The wear rate at 400 ℃ and 800 ℃ could reach 1.97×10^{-5} mm^3/N·m and 3.1×10^{-6} mm^3/N·m, respectively, which implies the broad applied potency and good service reliability in the harsh environment.

3.3. Wear morphology

Fig. 4 presents SEM micrographs of the worn surface after wear tests at room temperature with the load of 1–10 N. In Fig. 4(a1), the worn surface after the wear test at 1 N could be divided into the bright and dark regions which are recognized as the non-oxidation and oxidation zones (see the EDS mapping in the insert). As indicated by the arrows, some micro cracks and thin plate-like peels could be found in the oxidation zones, which reveals the delamination wear mechanism. In Fig. 4(a2-a3), there is a high density of local oxidation regions at the submicron scale (see the EDS mapping in the insert). Meanwhile, abrasive grooves along the sliding direction could be observed, which reveals the abrasive wear mechanism. Similar wear morphologies are found after wear tests at 2 N and 5 N, as shown in Fig. 4(b-c). It is

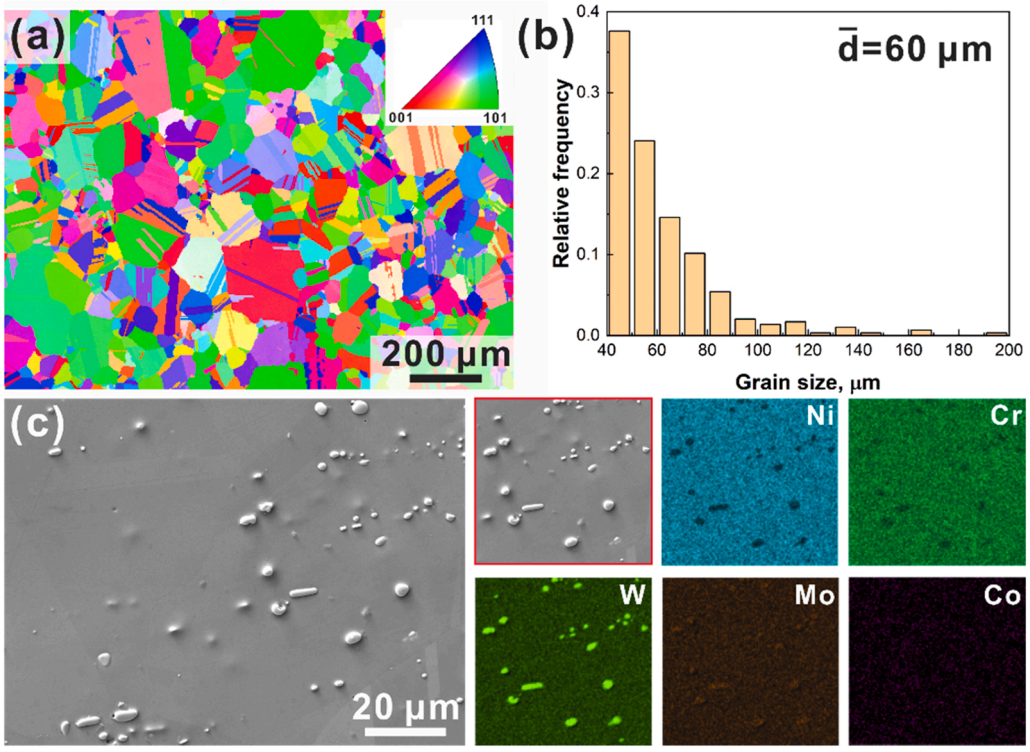

Fig. 1. (a) The IPF map of original microstructure of the Ni-27Cr superalloy and corresponding (b) grain size distribution. (c) Magnified SEM observation within one single grain and corresponding EDS mapping on the undissolved particles.

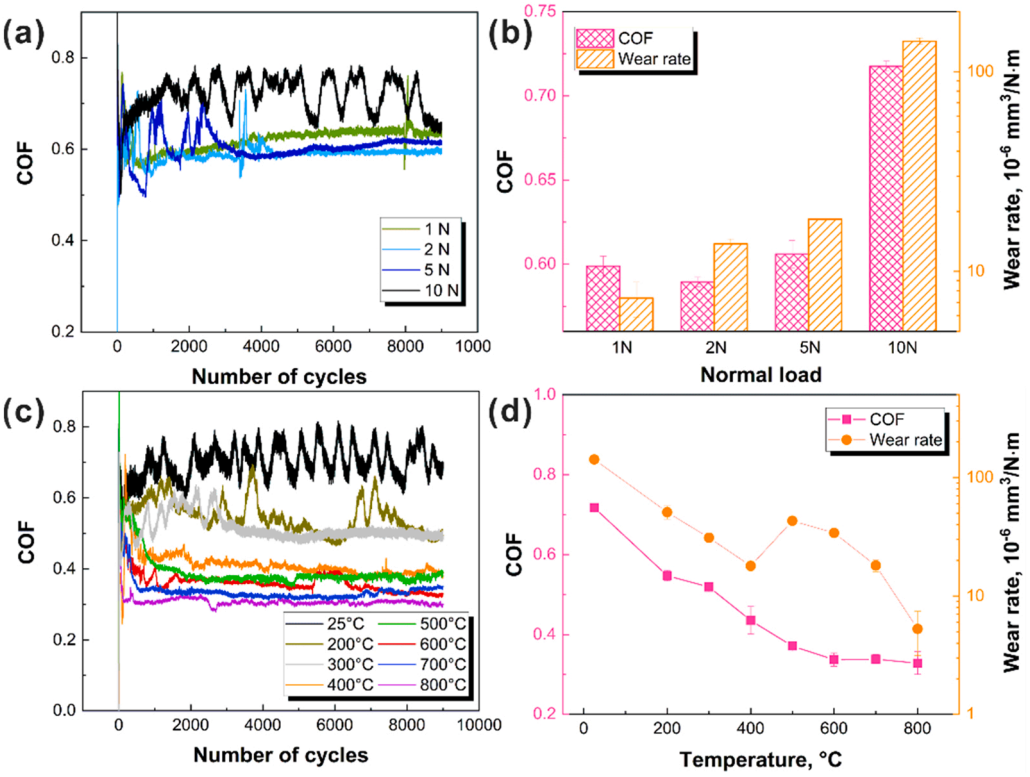

Fig. 2. (a) COF curves as a function of number of cycles at room temperature with different normal loads. (b) The average COF value and wear rate versus the normal load at room temperature. (c) COF curves as a function of number of cycles at varied temperature with the fixed load of 10 N. (d) The average COF value and wear rate versus the temperature.

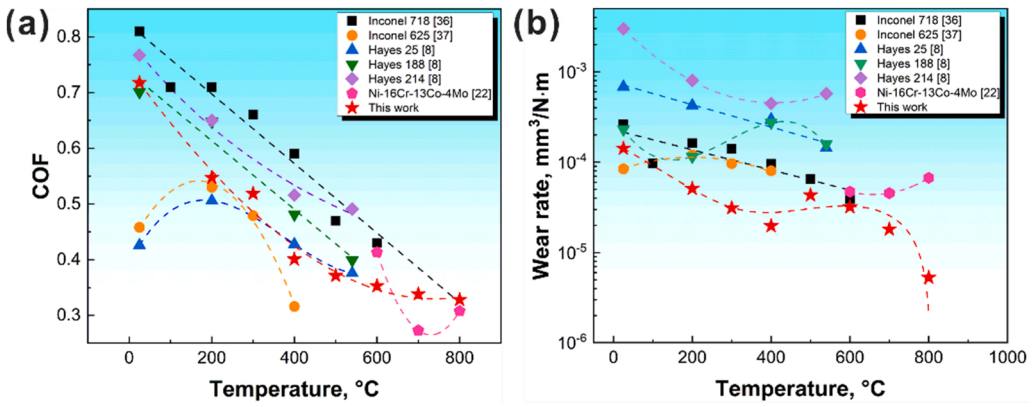

Fig. 3. Summary of (a) COFs and (b) wear rates for our Ni-27Cr sample and some commercial Ni-based superalloys from the literature [8,22,36,37].

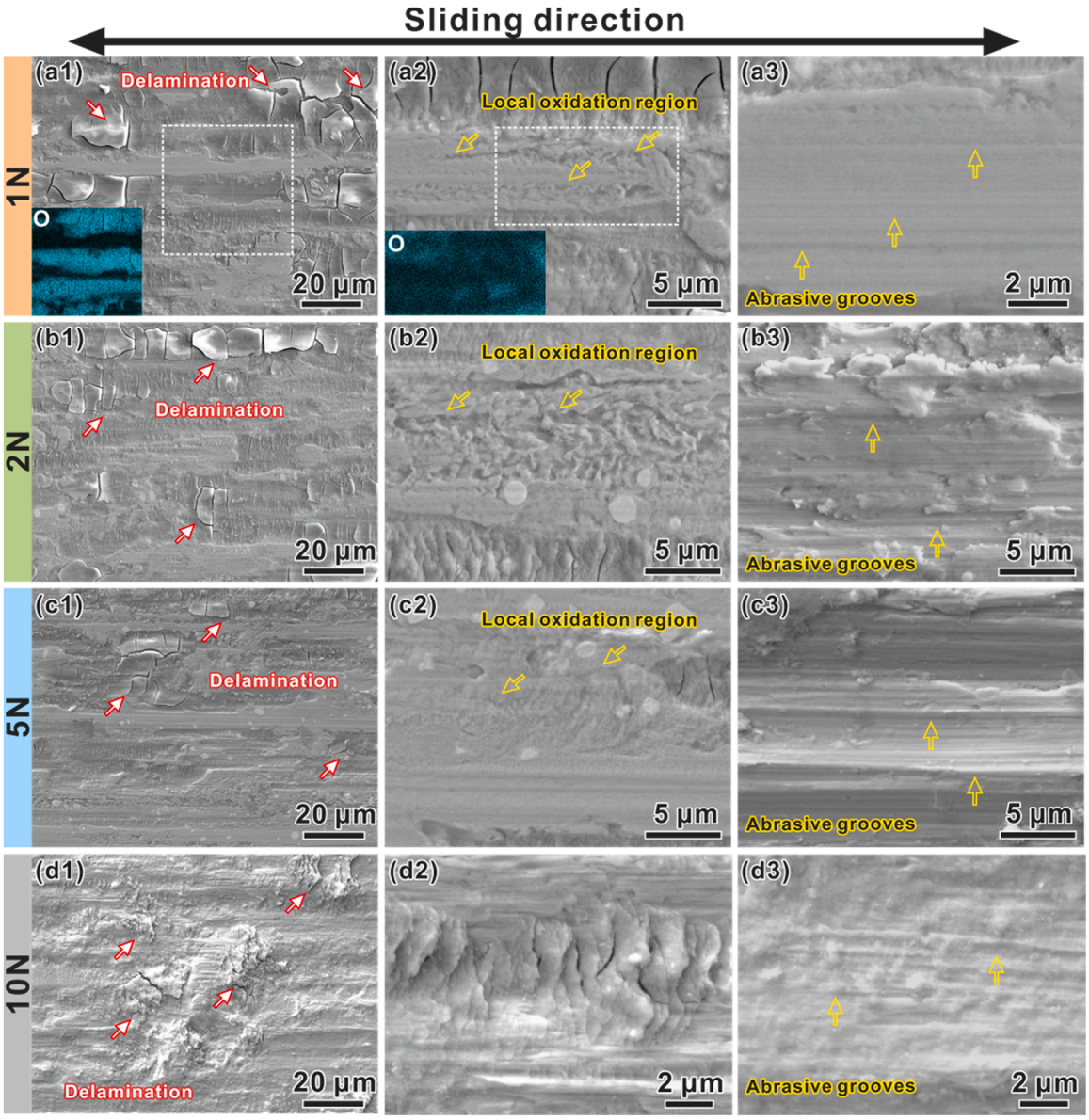

Fig. 4. SEM images of the worn surface and local damage morphology at room temperature with the normal load of (a1-a3) 1 N, (b1-b3) 2 N, (c1-c3) 5 N and (d1-d3) 10 N.

believed that the varied morphologies within the same wear scar could reflect the surface microstructure evolution and corresponding failure process under tribological loading. The frictional heating at the initial stage would contribute to the surface oxidation in the local regions. Then, the micro cracks would nucleate in the subsurface layer because the brittle nanograined oxides cannot accommodate the large tribo-induced plastic strain. Finally, the plate-like peels would form with the cracks manage to propagate towards the surface. Besides, the local adhesion in the oxidation regions leads to the high COF value of about 0.6. The difference of wear morphologies at 1–10 N is that the damage degree is much larger at 10 N. With increasing normal load to 10 N, the intensified delamination damage is marked as the pile-up of sheets and much deeper grooves.

Fig. 5 presents SEM micrographs of the worn surface after wear tests at varied temperature from 400 to 800 ℃ with the load of 10 N. After the wear test at 400 ℃, the worn surface is made up of the oxidation wear region (dark area) and abrasive wear region (bright area), as shown in Fig. 5(a). High-density wear debris and grooves could be found in the abrasive wear region (Fig. 5(a2)). Meanwhile, compacted tribo-layer was formed and underwent severe fragmentation in the oxidation wear region, as shown in Fig. 5(a3). Similar oxidation wear and abrasive wear regions appear on the worn surface after the wear test at 600 ℃ (Fig. 5(b1-b3)). However, the tribo-layer formed during the wear process seems to be more intact compared with that at 400 ℃. It is evident that some micro cracks accompanied with buckles and mild abrasive grooves instead of fragmented morphology appears on the tribo-layer (Fig. 5(b3)). After the wear test at 800 ℃, the scar width is smaller than that after the wear tests at 400 ℃ and 600 ℃, which is consistent with the wear rates in Fig. 2(d). Besides, the worn surface was completely covered by the tribo-layer (Fig. 5(c2)). Magnified observation in Fig. 5(c3) shows the abrasive grooves and local delamination along the sliding direction on the tribo-layer. Table 2 shows the atom fraction of oxygen in the oxidation wear and abrasive wear regions after wear tests at varied temperatures from 400 to 800 ℃ (For the sample worn at 800 ℃, the EDS data of abrasive wear regions was adopted in the delamination area in Fig. 5(c3)). With increasing temperature from 400 to 800 ℃, the oxygen content in the oxidized region remains the same at about 50%, while that in the abrasion region sharply increases from 6% to 48%. It indicates the degree of sintering and oxidation of the topmost tribo-layer is enhanced with increasing temperature, which could result in a reduction in COF.

Table 2
Atomic fractions of oxygen in the worn surface by EDS.

Temperature	25 ℃	400 ℃	600 ℃	800 ℃
Oxidation region	51.78%	49.36%	51.42%	50.46%
Abrasion region	2.64%	6.3%	41.3%	48.22%

3.4. Subsurface microstructure

The cross-sectional microstructure below the sliding surface at 25–800 ℃ were presented in Figs. 6–9. It is worth to note that all the TEM samples were from the abrasion wear regions. For the sample worn at room temperature, the cross-sectional region could be separated into the nanocrystalline layer (NCL) and deformed coarse grain (CG) region according to the contrast of grain morphology (Fig. 6(a)). At the depth of 5–10 μm from the surface, dislocation tangles and micro bands are both observed. Fig. 6(b) shows the magnified observation of the well-developed plate-like micro bands with a thickness of about 100 nm, as

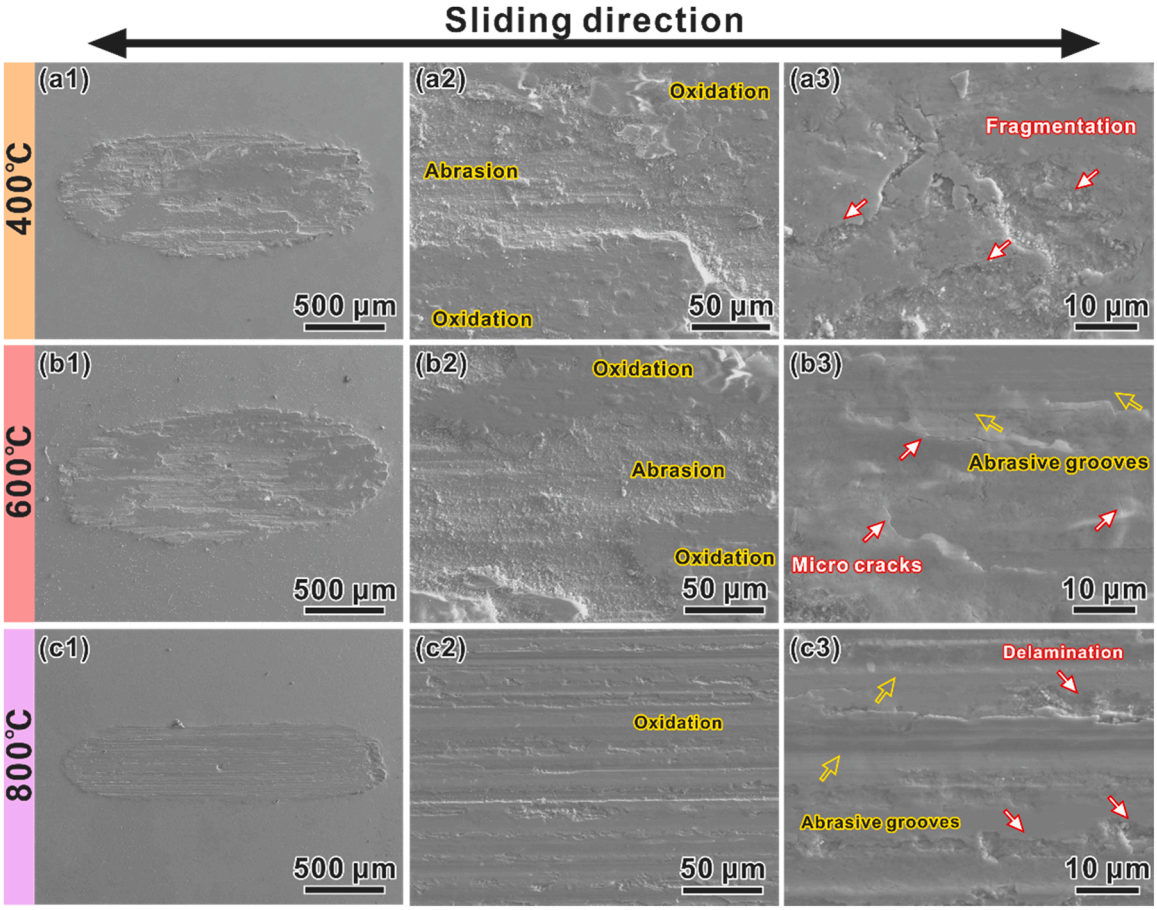

Fig. 5. SEM images of the worn surface and local damage morphology at varied test temperatures: (a1-a3) 400 ℃, (b1-b3) 600 ℃, (c1-c3) 800 ℃.

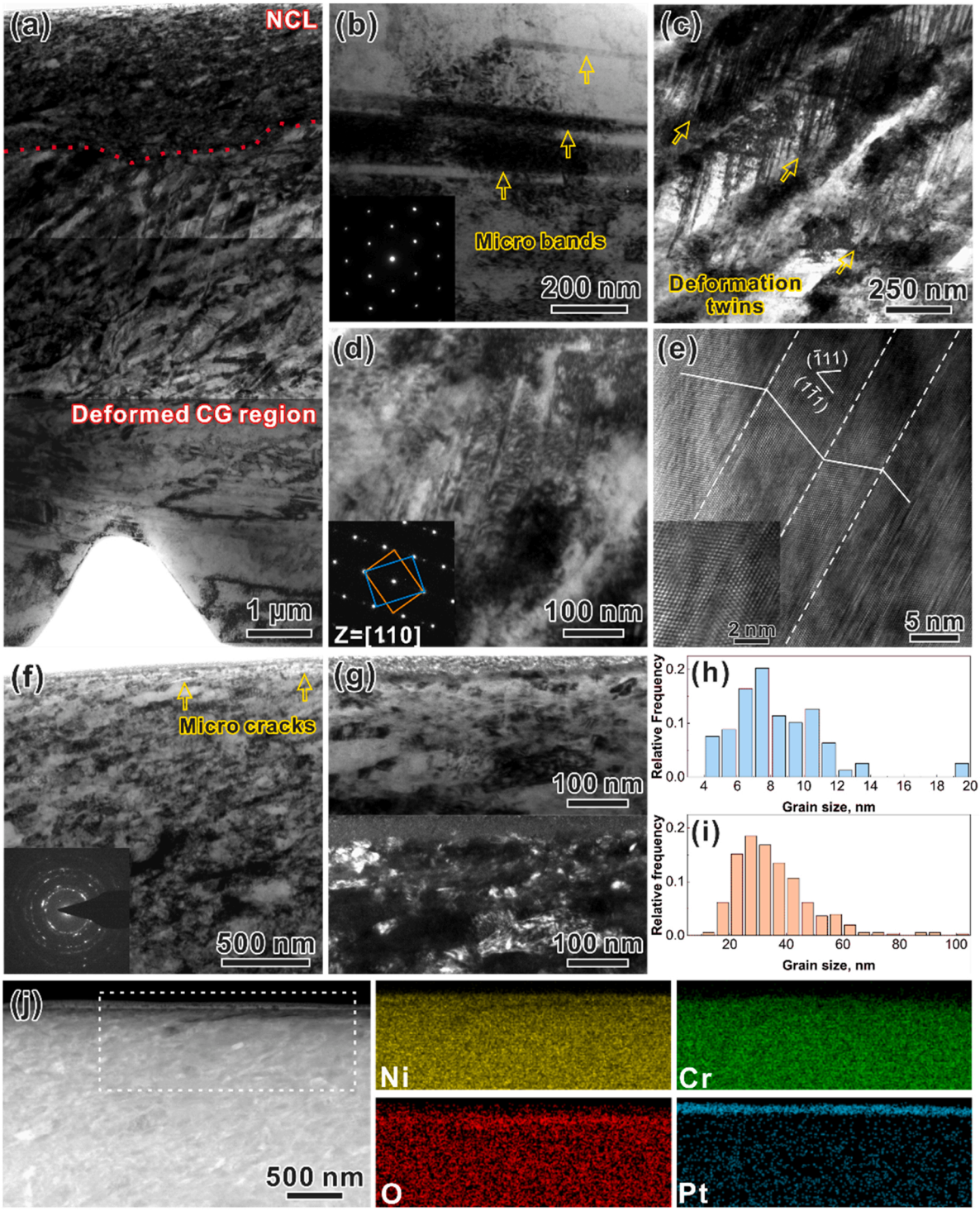

Fig. 6. Cross-sectional TEM characterization of the worn subsurface structure for the Ni-27Cr superalloy during dry sliding at 10 N after 9000 cycles at room temperature. (a-c) Bright-field TEM images of the (a) whole subsurface microstructure, (b) micro bands and (c) deformation twins with corresponding selected area electron diffraction (SAED) patterns. (d and e) Magnified (d) bright field TEM and (e) HRTEM images of the nanotwins with corresponding SAED patterns. (f) A magnified bright field TEM image on the whole NCL. (g) Bright/dark field TEM images of equiaxed ultrafine nanograins in the topmost layer. (h and i) Grain size distributions of the region with depth from 2.5 μm to 80 nm and the topmost region with depth less than 80 nm. (j) A HAADF-STEM image of the topmost layer and corresponding EDS mapping of the selected area (dashed box).

indicated by the arrows. At the depth of 2.5–4.5 μm from the surface, high-density lamellar structure with an average thickness of about 10 nm could be found between the micro bands (Fig. 6(c)). Magnified bright field TEM and HRTEM observation and corresponding selected area diffraction pattern in Fig. 6(d-e) further verifies the formation of deformation nanotwins during the sliding wear process. With decreasing depth from 2.5 μm to 80 nm, the NCL consists of elongated nanograins with the average grain size of about 35 nm (Fig. 6(i)). As indicated by the arrows in Fig. 6(f), some micro cracks are identified at the grain boundaries. It is believed that crack propagation toward the worn surface would lead to the debris formation during the sliding wear process. Finally, equiaxed ultrafine nanograins are formed in the top surface

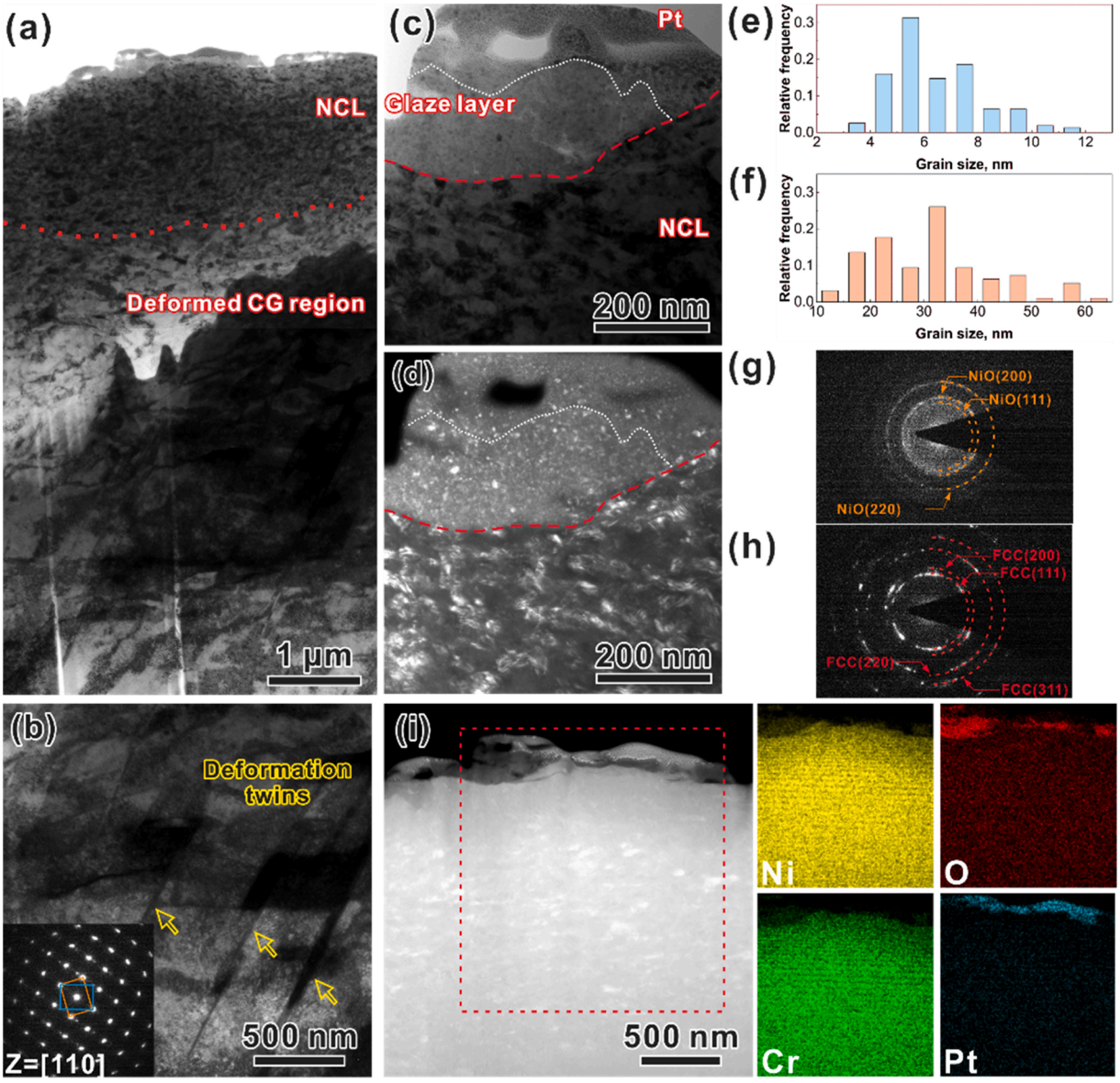

Fig. 7. Cross-sectional TEM characterization of the worn subsurface structure for the Ni-27Cr superalloy during dry sliding after 9000 cycles at 400 ℃. (a and b) Bright-field TEM images of the (a) whole subsurface microstructure and (b) deformation twins with corresponding SAED patterns. (c and d) Magnified (c) bright and (d) dark field TEM images of the topmost layer. (e-h) Grain size distributions and SAED patterns of the (e, g) glaze layer and (f, h) NCL. (i) A HAADF-STEM image of the topmost layer and corresponding EDS mapping of the selected area (dashed box).

layer of the sample and the mean grain size is approximately 8 nm (Fig. 6(g-h)). The corresponding EDS element mapping of the selected area (white dashed box) in Fig. 6(j) reveals that the topmost surface layer is oxygen-rich, which contributes to the grain refinement degree during the wear process [38–40].

Similar to the results in Fig. 6, the cross-sectional region of the sample worn at 400 ℃ could be also separated into the NCL and deformed CG region (Fig. 7(a)). In Fig. 7(b), some deformation nanotwins accompanied with dislocation tangles could be observed in the deformed CG region at the depth of 2.5–4.5 μm from the surface. In the topmost surface, only part of the NCL is covered by the glaze layer, as indicated by the TEM bright/dark field images (Fig. 7(c-d)). The fragmented morphology of the glaze layer implies that it tends to be ground off during the wear process at 400 ℃, which is consistent with the SEM observation in Fig. 5(b). There is an evident transition of grain size and morphology from the glaze layer to the NCL across the interface (red dashed line in Fig. 7(c-d)). The average gran sizes of the equiaxed nanograins in the glaze layer and elongated nanograins in the NCL are 7 and 32 nm, respectively (Fig. 7(e-f)). The EDS mapping of the selected area (red dashed box) in Fig. 7(i) and corresponding SAED patterns (Fig. 7(g)) reveal that the glaze layer is mainly composed of NiO compound, while the NCL still exhibits the FCC structure indicated by the SAED pattern (Fig. 7(h)).

For the sample worn at 600 ℃, the cross-sectional region still consists of the NCL and deformed CG region (Fig. 8(a)). At the depth of about 6 μm from the surface, the appearance of deformation nanotwins implies that twinning behavior could be still activated during the sliding wear process at 600 ℃. In the topmost surface, a dense glaze layer with the average layer thickness of about 40 nm is formed upon the NCL, which is accompanied with the appearance of some hillocks at submicron scale (see the insert in Fig. 8(a)). According to the micro crack found at the hillock (Fig. 8(c)), the oxidation layer at 600 ℃ has a tendency to break and peel off during the sliding wear process. There is also a large difference in the grain size between the glaze layer and NCL. The average gran sizes of the equiaxed nanograins in the glaze layer and elongated nanograins in the NCL are 8 and 35 nm, respectively (Fig. 8(e-

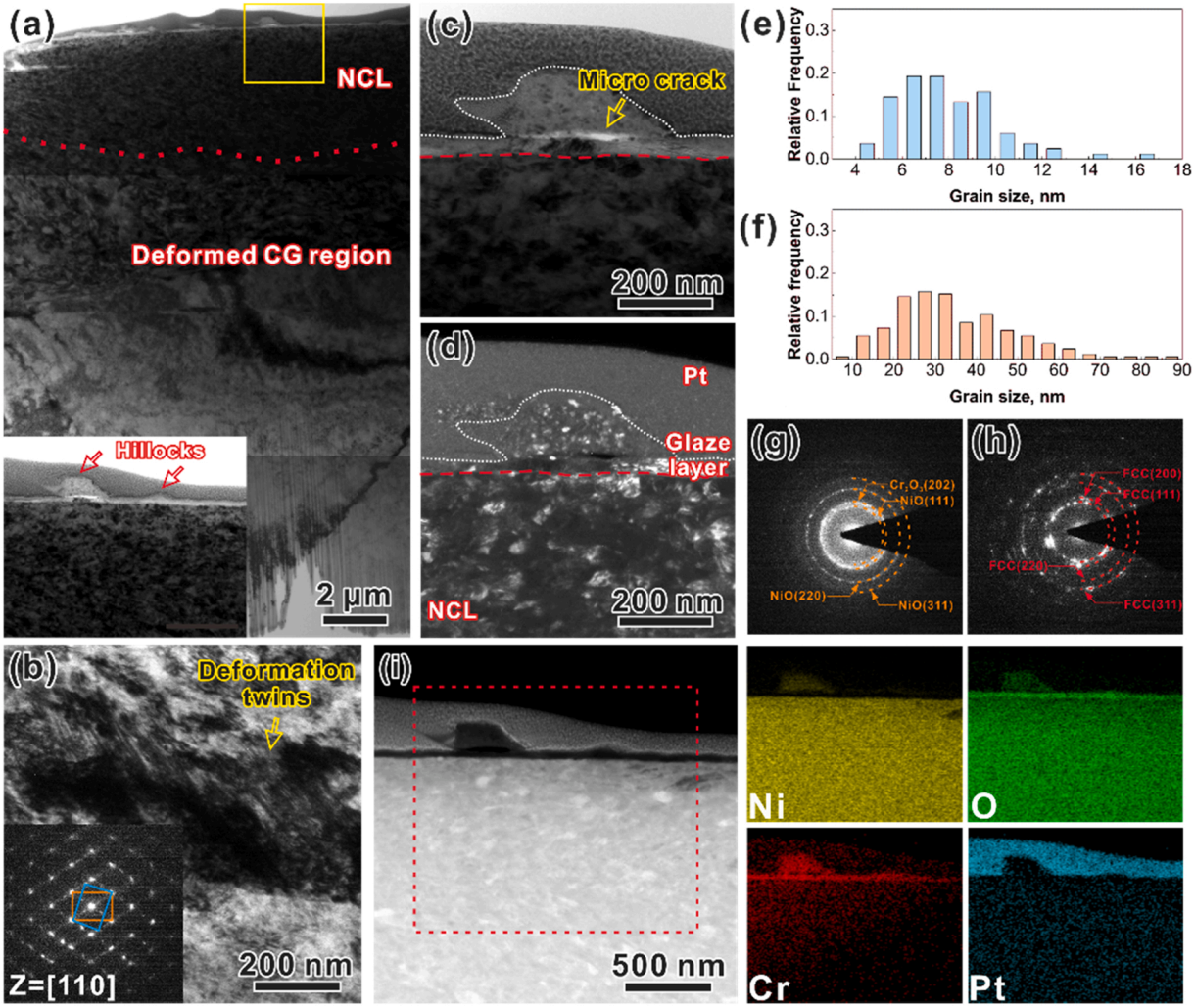

Fig. 8. Cross-sectional TEM characterization of the worn subsurface structure for the Ni-27Cr superalloy during dry sliding after 9000 cycles at 600 ℃. (a and b) Bright-field TEM images of the (a) whole subsurface microstructure and (b) deformation twins in the deformed CG region. The insert is a magnified TEM image of the hillocks in the solid box. (c and d) Magnified (c) bright and (d) dark field TEM images of the topmost layer. (e-h) Grain size distribution and SAED patterns of the (e, g) glaze layer and (f, h) NCL. (i) A HAADF-STEM image of the topmost layer and corresponding EDS mapping of the selected area (dashed box).

f)). The EDS mapping in Fig. 8(i) show that the thin and compact glaze layer is a Cr-rich oxide layer. The whole oxidation region mainly consists of ultrafine nanograined NiO and Cr_2O_3, as shown in Fig. 8(g). Beneath that, oxygen was also detected in the NCL indicating the occurrence of internal oxidation, but the matrix alloy remains the single FCC structure (Fig. 8(h)).

For the sample worn at 800 ℃, the cross-sectional region consists of the glaze layer, dynamic recrystallization (DRX) layer and deformed CG region (see Fig. 9(a)). The glaze layer greatly increases dramatically to about 3 μm with increasing the temperature to 800 ℃. Fig. 9(b1) shows the corresponding HAADF-STEM observation of the cross-sectional microstructure, which shows an evident difference of the image contrast within the glaze layer. The EDS mapping results of the selected area (white dashed box) in Fig. 9(b1) reveal two points: (1) there is a Cr-rich oxide region with an average thickness of about 500 nm locating between the Ni-rich oxide region and DRX layer along the thickness direction, as indicated by the arrows in Fig. 9(b2-b3). It is believed that the formation of continuous Cr-rich oxide layer manage to prevent further oxidation of the substrate. According to the magnified observation and SAED patterns in Fig. 9(c-f), the Ni-rich and Cr-rich oxide regions consist of nanograined $NiCr_2O_4$ and Cr_2O_3, respectively. The average grain size of the ultrafine nanograins in the glaze layer is about 18 nm which is larger than that of the samples worn at 400 ℃ and 600 ℃ (Fig. 9(g)). It could be attributed to the temperature effect on the grain growth during the sliding process. (2) It is surprising to find several unoxidized regions in the glaze layer which are fully enclosed by the Cr-rich oxide layers (see the arrows in Fig. 9(b4)). The EDS line scanning result (Fig. 9(b5)) of the selected area in the insert of Fig. 9(b1) could further justify the conclusion and the average thickness of the closed Cr-rich oxides is obtained as about 100 nm. Meanwhile, combined with the TEM observation in Fig. 9(h), the unoxidized DRX regions consist of ultrafine grains. Furthermore, multiple dislocation segments within the single DRX grain reveals that the isolated DRX regions can undertake large plastic deformation during the sliding process (Fig. 9(i)). Compared to the DRX layer, the DRX regions in the glaze layer is closer to the worn surface. Due to the difference of applied stress and plastic strain accumulation, the grain refinement degree of the DRX regions in the glaze layer is larger than that of the DRX layer (Fig. 9(j)). The average grain sizes of the DRX regions in the glaze layer and the DRX layer are 140 and 200 nm according to the grain distribution in Fig. 9(k-l).

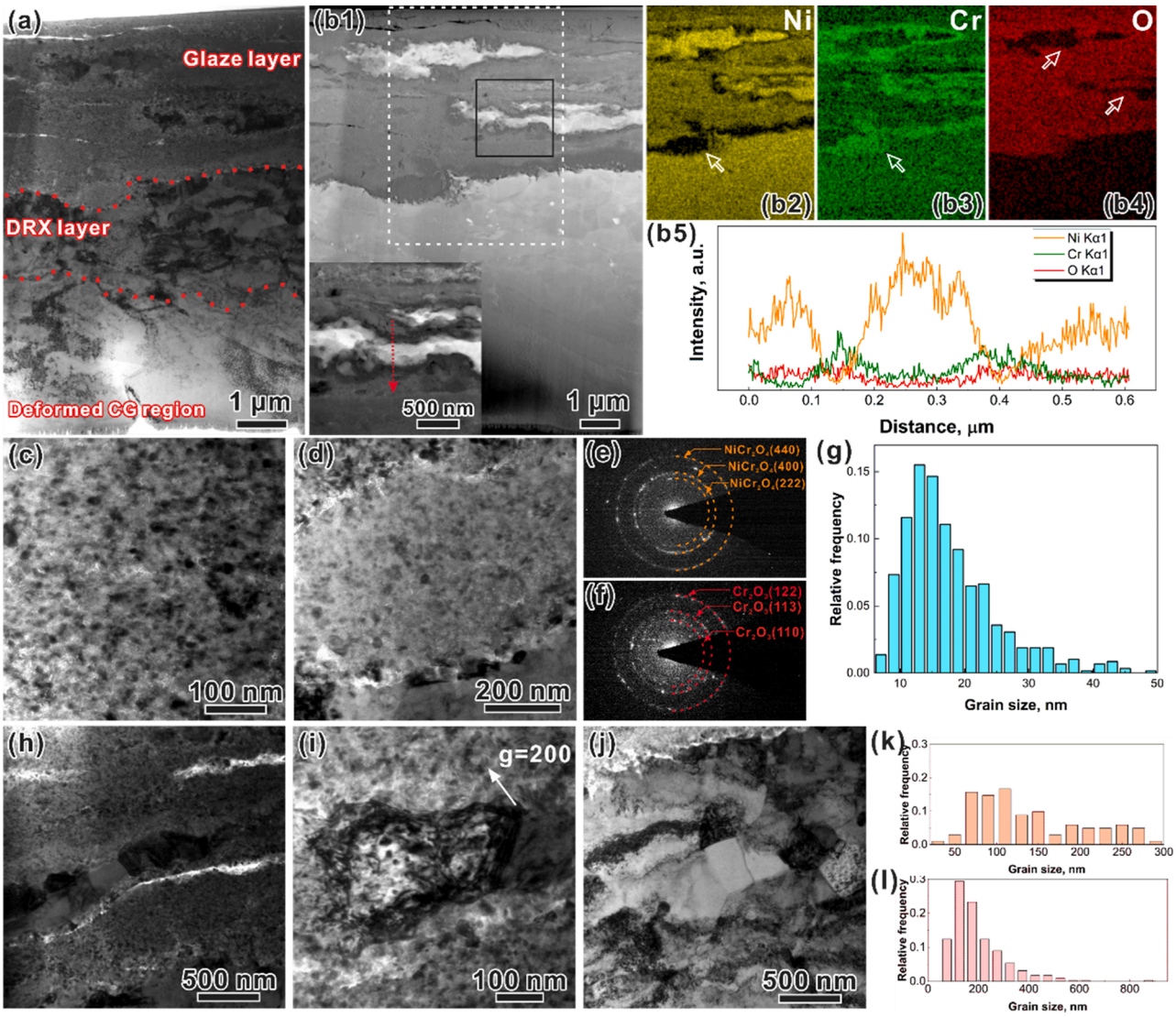

Fig. 9. Cross-sectional TEM characterization of the worn subsurface structure for the Ni-27Cr superalloy during dry sliding after 9000 cycles at 800 ℃. (a) A Bright-field TEM image and (b1) a corresponding HAADF-STEM image of the whole subsurface microstructure with corresponding EDS (b2-b4) mapping and (b5) line scanning results of the selected regions (dashed box and arrow). The insert is a magnified STEM image of the solid box in the glaze layer. (c-f) Magnified TEM images and SAED patterns of the (c, e) Ni-rich and (d, f) Cr-rich oxide layers. (g) Grain size distribution of the glaze layer. TEM bright images of the (h) unoxidized regions, (i) one DRX grain in the glaze layer and (j) DRX layer. Grain size distributions of the unoxidized regions in the (k) glaze layer and (l) DRX layer.

4. Discussion

4.1. Tribo-induced structural and chemical alterations at room/elevated temperatures

Compared with the commercial Ni-based superalloys, our Ni-27Cr superalloy has a much higher Cr content, which greatly affect the twinning behavior, grain refinement mechanism and oxidation behavior at room/elevated temperatures.

4.1.1. Tribo-induced twinning behavior

The cross-sectional characterization demonstrates that tribo-induced deformation nanotwins have excellent structural stability against wear at 25–600 ℃. Up to 800 ℃, the tribo-induced nanotwins are absent, replaced by dislocation activities in the subsurface layer. According to Eq. (1), adding 27 at% Cr could lead to a decreased SFE of Ni-Cr binary alloy from 125 $mJ{\cdot}m^{-2}$ to 80 $mJ{\cdot}m^{-2}$ and therefore promotes deformation twinning in the coarse-grained Ni-27Cr superalloy (The absolute SFE value of Ni-27Cr superalloy needs further investigation by the

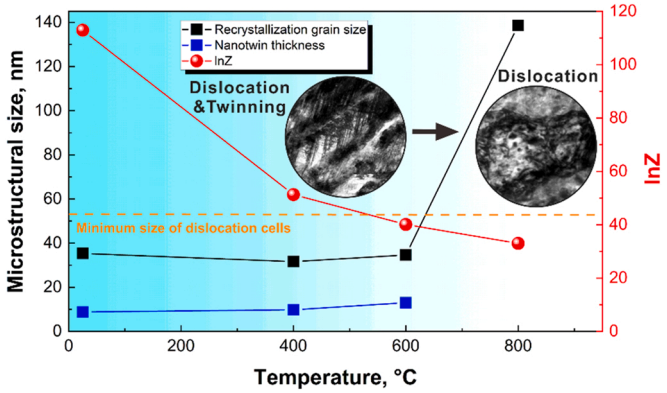

Fig. 10. DRX grain size, nanotwin thickness and lnZ versus the wear temperature for the Ni-27Cr superalloy.

means of DFT in the future) [35,41]. The average thickness of deformation nanotwin slightly increases from 8 nm to 13 nm from 25 ℃ to 600 ℃, as shown in Fig. 10. It is believed that the deformation twinning could still be activated at 400–600 ℃ due to the coupled effect of SFE and strain rate [42,43]. Low-energy TBs serve as effective barriers to dislocation motion for strengthening the superalloy at elevated temperatures and can also accommodate tribological strains by absorbing dislocations via TB interactions with glide dislocations [44,45]. Besides, the solution-strengthening elements such as Cr and Co could provide a robust barrier in stabilizing the twin boundaries by forming elemental segregation or precipitations [46,47]. At 800 ℃, the absence of twins could be attributed to the increased SFE and material softening, which dose not favor the slip of partial dislocations [48].

4.1.2. Tribo-induced grain refinement mechanism

In order to reveal the temperature effect on the tribo-induced grain refinement mechanisms, the Zener-Hollomon parameter (Z) was introduced [49], as defined by:

$$Z = \dot{\varepsilon}\exp(Q/RT) \tag{1}$$

where $\dot{\varepsilon}$ is the strain rate, R is the gas constant, Q is the related activation energy for deformation and T represents the deformation temperature. Here, the activation energy of pure Ni for grain boundary migration (274 kJ/mol) is adopted for simplicity [50]. The strain rate was estimated as 10 s^{-1} according to our previous work on the measurement of sliding strain rates [51]. The value of lnZ decreases from 20 to 5 with increasing the deformation temperature from 25 ℃ to 800 ℃, as shown in Fig. 10. Considering that the dislocation cell sizes (D_{dc}) depends on the applied shear stress (τ) according to

$$D_{dc} \approx \frac{KGb}{\tau} \tag{2}$$

where K is a constant as 10, G is the shear modulus, b is the Burgers vector (0.2492 nm for Ni here). If the applied shear stress reaches the upper limit (G/30), the recrystallization grain size dominated by the dislocation behavior would decrease to a minimum value as about 53 nm, as indicated by the horizontal dashed line in Fig. 10. It is obvious that the average recrystallization grain size at 25 ℃ to 600 ℃ remains constant as about 35 nm, which is smaller than the minimum size of dislocation cells. While the recrystallization grain size at 800 ℃ (138 nm) is much larger than the minimum value (The data is extracted in the unoxidized regions of the glaze layer). It is deduced that there is a transition of grain refinement mechanism with increasing the temperature from 25 ℃ to 800 ℃.

For the Ni-27Cr alloy sliding from 25–600 ℃ (i.e. with high Z), the dislocation/twinning interaction dominates the refinement of coarse grains. The Ni-27Cr superalloy has a strong tendency to form planar dislocation arrays which would further evolve into the micro bands (Fig. 6(b)), in analogy to that in the Al-Mg alloys [52] and high manganese steels with low SFEs [53]. Fig. 11 shows the magnified micrograph on the interaction between the micro bands and deformation twins for the sample sliding at 25 ℃. It is found that the deformation twins with lengths of 1.5–2 μm indicated by the yellow solid arrows manage to penetrate several micro bands (white dashed lines). Besides, the twin boundaries have a 4° deflection to maintain the favored orientation for continuous twinning (see the SAED in Fig. 11 c). At the same time, high-density nanotwins with lengths of hundreds of nanometers indicated by the yellow dashed arrows are constrained by the adjacent micro bands. It contributes to the further subdivision of the grain into the rhombic-shaped nanoscale domains (see the red box in Fig. 11a). Then, dislocation tangles are developed within the domains and evolve into randomly orientated grains. For the Ni-27Cr alloy sliding at 800 ℃ with a relatively low Z, grain refinement is dominated by the dislocation activities. The dislocation tangles gradually transform into subgrain boundaries and further into high-angle grain boundaries [54]. The contribution of deformation twinning to grain refinement is absent and the combination of frictional/ambient heating will promote the DRX grain growth at 800 ℃. In a word, from 25 ℃ to 800 ℃, there is a transition of grain refinement mechanisms from dislocation/twinning interaction to dislocation activities when lnZ decreases from 20 to 5. It is worth noting that the role of dislocation density in grain refinement is important and the dislocation density measurement will be carried in the future.

4.1.3. Tribo-oxidation behavior

For the commercial Ni-based superalloys, the glaze layer basically consists of homogeneous nanostructured oxides (e.g. NiO, CoO, Cr_2O_3 and $NiCr_2O_4$) [20,22,55]. For our Ni-27Cr alloy sliding from 25 ℃ to 800 ℃, there is a transition of tribo-induced oxidation behavior from insufficient oxygen diffusion to the formation of a fragmented glaze layer consisting of homogeneous nanograined NiO and a thin Cr_2O_3 layer and finally to the formation of a heterogeneous composite glaze layer consisting of nanograined $NiCr_2O_4$ and unoxidized UFG matrix wrapped with Cr_2O_3.

During the preheating process, static oxidation process would occur at the sample surface. Then, wear debris were generated in the wear process and a part of them evolve into the glaze layer after repeated welding and fracture [56–59]. For our Ni-27Cr superalloy, there is only slight diffusion of oxygen in the topmost surface at 25 ℃ because the oxygen diffusion rate is relatively low at room temperature. The glaze layer formed at 400 and 600 ℃ both exhibit fragmented morphologies (see Fig. 5). The difference is the formation of a thin and continuous Cr-rich oxidation layer formed in the inner side of the glaze layer at 600 ℃. Because the diffusion/oxidation rate is enhanced at higher temperatures and the driving force of Cr_2O_3 is greater than that of Ni

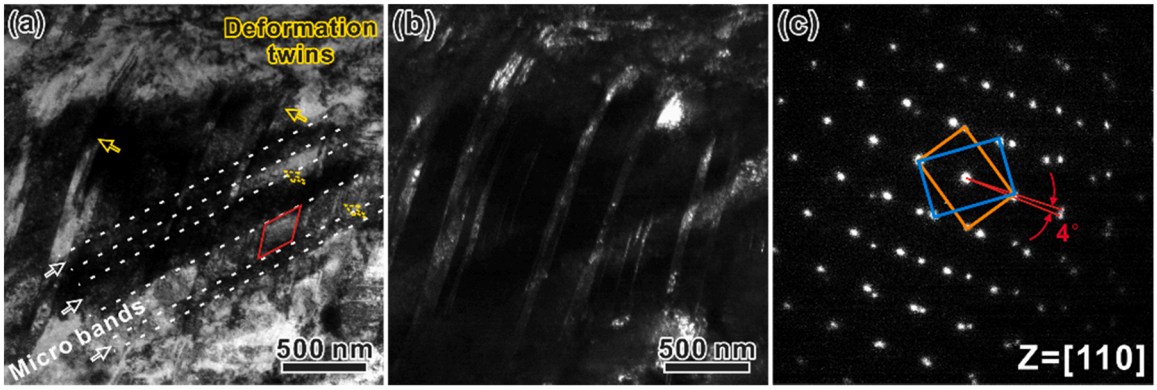

Fig. 11. Magnified (a) bright and (b) dark field TEM images of twin boundaries-dislocation interaction and (c) corresponding SAED for the Ni-27Cr superalloy worn after 9000 cycles at 25 ℃.

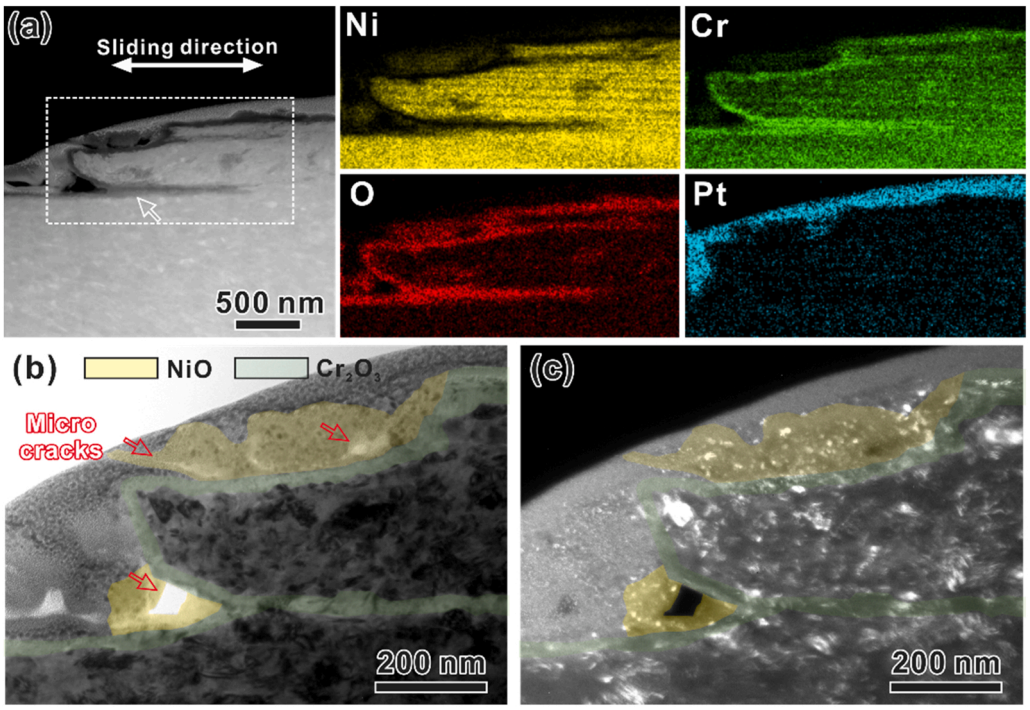

Fig. 12. (a) A STEM-HADDF image on the oxidization layer of the Ni-27Cr superalloy after dry sliding after 9000 cycles at 600 ℃ and corresponding EDS mapping. (b) Magnified (b) bright and (c) dark field TEM observation on the micro cracks within the fragmented NiO layers.

oxide [22,60]. This is further substantiated by TEM characterization of another cross-section after dry sliding at 600 ℃ (Fig. 12). The whole NCL exhibits a step-like morphology along the thickness direction (Fig. 12(a)) and is fully covered by a Cr-rich oxidation layer (green area in Fig. 12(b-c)). Similar to the results in Fig. 8, some fragmented NiO regions (yellow area in Fig. 12(b-c)) accompanied with several micro cracks (red arrows) appears outside of Cr-rich oxidation layer. Even though external Cr_2O_3 is able to prevent oxygen from diffusing into the substrate alloy, internal Cr-rich oxidation in the NCL could still be found, as indicated by the arrow in Fig. 12(a). It implies that the crack propagation along the sliding direction contributes to the formation of Cr-rich oxidation layer along the same direction in the matrix.

The formation of heterogeneous composite glaze layer at 800 ℃ is intimately correlated to the intentional addition of high Cr content. First, it is reasonable that enough Cr is triggered to diffuse outward to form the Cr_2O_3 layer in the early stage [19,20]. Second, the tribo-induced cracking and pile-ups would contribute to the oxygen penetration along the propagation direction and plastic flow direction, respectively [55,61]. Residual Cr_2O_3 clusters should exist in the glaze layer. Thus, the high Cr content significantly increases the possibility that the retained discrete Cr_2O_3 layers completely enclose a small part of the matrix in the glaze layer. Furthermore, the matrix-Cr_2O_3 composites are sintered within the glaze layer instead of being removed [62]. Finally, the unoxidized regions would experience the DRX process under the protection of the dense Cr_2O_3 shells. In contrast, only several Cr-rich banded clusters appear in the homogeneous nanograined glaze layer for those Ni-based superalloys with relatively low Cr content (16 at%) during the sliding process [22]. The chemical origins for the heterogeneous composite glaze layer at 800 ℃ merit further in-depth investigations of the early stage sliding.

4.2. Wear-resistant subsurface nanotwins and heterogeneous composite glaze layer

Our coarse-grained Ni-27Cr superalloy share the same wear mechanisms (abrasive/oxidation) but exhibits superior wear resistance from 25 ℃ to 800 ℃, compared to the precipitation-strengthening superalloys such as Inconel 718/625. Typically, sliding at elevated temperatures leads to the homogeneous glaze layer (hard but brittle) and adjacent NCL for the traditional Ni-based superalloys [22,56,63]. On the one hand, the dissolution of strengthening phases in the matrix causes the softening of the subsurface layer, and the increased strain incompatibility between the glaze layer and NCL would lead to the crack nucleation at the layer interface [63]. On the other hand, concentrated plastic deformation on the topmost region would lead to strain localization. Then, the fresh glaze layer tends to be broken and removed as the abrasive debris. While for our Ni-27Cr superalloy, the key of high wear resistance lies in the activation of twin strengthening and formation of heterogeneous composite glaze layer.

First, tribo-induced twin strengthening contributes to the high wear resistance at room/intermediate temperatures. The deformation nanotwins become an important part of the wear-induced gradient nanostructure at 25 ℃. There is a continuous structural refinement from the micro bands/dislocation tangles to the nanograins along the thickness direction, as shown in Fig. 13(a). The gradient yield stress of the subsurface gradient nanostructure could match the distribution of applied tribological stress [27,64]. Then, plastic deformation could be sustained within a thicker surface layer and smaller plastic strain gradient would be induced in the subsurface gradient nanostructure. Thus, strain localization and severe material peel-off are avoided, which leads to the enhanced wear resistance at 25 ℃. The activated twinning behavior could further enhance the subsurface grain refinement through the dislocation-twinning interaction, especially at the intermediate temperatures. Even though the topmost glaze layer is not intact, nanograins with high hardness in the NCL and retained nanotwins with superior thermal stability and good strain hardening ability in the deformed CG region would give strong support against sliding and then reduce the wear rate of Ni-27Cr superalloy at 400 ℃, as shown in Fig. 13 (b).

Second, the resultant heterogeneous composite glaze layer is decisive for the remarkable wear resistance at 800 ℃. This can be interpreted from the following two aspects. (i) The grain boundary mobility is retarded due to the pinning effect of alloy elements [65]. Thus, the

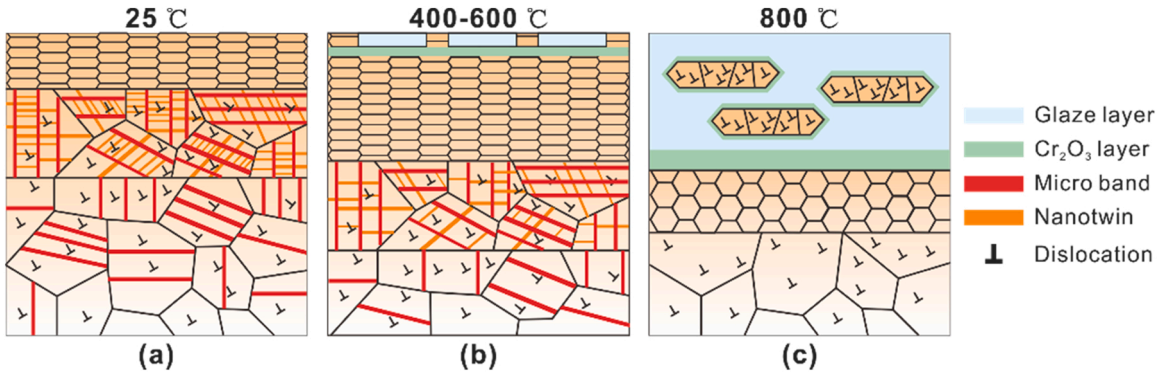

Fig. 13. Schematic illustration of microstructure evolution for the Ni-27Cr superalloy worn at (a) 25 ℃, (b) 400–600 ℃ and (c) 800 ℃.

nanograined glaze layer tends to remain stable during the thermo-mechanical coupling process, which would restrain the generation of wear debris. $NiCr_2O_4$ as the main oxides in the glaze layer has a spinel crystalline structure which is beneficial to reduce the friction [20]. Thus, the intact and thick glaze layer acts as a lubricant and barrier during the wear process, leading to the decreased COF at 800 ℃. (ii) The glaze layer consisting of nanograined oxides-UFG matrix could be regarded as a typical heterogeneous structure, as schematically shown in Fig. 13(c). The ultrafine nanograined $NiCr_2O_4$ and Cr_2O_3 contributes high strength to the glaze layer, and the unoxidized DRX regions maintain good ductility by the intrinsic strain hardening ability. Under tribological loading, the strain partitioning between the soft/hard zones would occur where the soft unoxidized regions could undertake much higher plastic strain than that of the surrounding nanograins [66]. The hetero-deformation induced (HDI) strengthening and hardening [67] would improve the ductility of the whole glaze layer and corresponding wear resistance of the sample. Compared to the nanocomposite consisting of nanocrystals and amorphous oxides [25], our heterogeneous composite glaze layer consisting of nanograined oxides and UFG matrix are supposed to have a much larger capacity to accommodate tribological strains. We propose that the rational design of strong and ductile heterogeneous composite glaze layer is a new strategy for designing wear-resistant superalloys at elevated temperatures. It is worth noting that the effect of material softening and increased fracture toughness at elevated temperature on the tribological properties needs further investigation [68].

5. Conclusions

In summary, a novel coarse-grained Ni-27Cr based superalloy was developed via tribo-induced twin strengthening and formation of strong and ductile composite glaze layer with heterostructures. The salient conclusions are drawn as follows:

(1) Compared to the commercial superalloys, the Ni-27Cr superalloy exhibit superior wear resistance at 25–800 ℃. The wear rates at 400 ℃ and 800 ℃ could reach 1.97×10^{-5} $mm^3/N{\cdot}m$ and 3.1×10^{-6} $mm^3/N{\cdot}m$, respectively.
(2) The damage degree of wear scars increases with increasing the normal load from 1 N to 10 N at room temperature. The degree of sintering and oxidation of the topmost tribo-layer is enhanced with increasing the temperature from 25 ℃ to 800 ℃.
(3) Tribo-induced deformation nanotwins with superior structural stability appear after wear at 25–600 ℃. From 25–800 ℃, there is a transition of deformation-induced grain refinement mechanism from dislocation-twinning interaction to dislocation behavior when lnZ decreases from 20 to 5. Besides, there is a transition of tribo-oxidation behavior from insufficient oxygen diffusion to the formation of a fragmented glaze layer consisting of nanograined NiO and a thin Cr_2O_3 layer and finally to the formation of a heterogeneous composite glaze layer consisting of nanograined $NiCr_2O_4$ and ultrafine grained matrix. The heterogeneous composite glaze layer stems from the high-Cr-triggered closure of Cr_2O_3 layers between hard and soft domains during tribological loading.
(4) At 25–600 ℃, tribo-induced deformation nanotwins contribute to the formation of gradient nanostructure and promote the subsurface grain refinement, alleviating the strain localization. At 800 ℃, the heterogeneous composite glaze layer could accommodate large tribological strains by HDI strengthening and hardening, providing a novel design pathway for wear-resistant superalloys at elevated temperatures.

Declaration of Competing Interest

The authors declare that they have no known competing financial interests or personal relationships that could have appeared to influence the work reported in this paper.

Data Availability

Data will be made available on request.

Acknowledgements

X. Chen would like to acknowledge financial supports from National Natural Science Foundation of China (Grant No. 51931003 and 52001165), Natural Science Foundation of Jiangsu Province, China (Grant No. BK20200475) and the Fundamental Research Funds for the Central Universities (Grant No. 30921011215). F. Liang acknowledges financial supports from the Fundamental Research Funds for the Central Universities (Grant No. 30922010401) and the Jiangsu Funding Program for Excellent Postdoctoral Talent (Grant No. 2022ZB2251). The authors are thankful for the technical support from Jiangsu Key Laboratory of Advanced Micro&Nano Materials and Technology, and the Materials Characterization Facility of Nanjing University of Science and Technology.

Statement of Originality

The proposed content are original and not involving plagiarism with copyright infringement issues.

References

[1] Amato KN, Gaytan SM, Murr LE, Martinez E, Shindo PW, Hernandez J, et al. Microstructures and mechanical behavior of Inconel 718 fabricated by selective laser melting. Acta Mater 2012;60:2229–39.

[2] Chen J, Chen J, Wang Q, Wu Y, Li Q, Xiao C, et al. Enhanced creep resistance induced by minor Ti additions to a second generation nickel-based single crystal superalloy. Acta Mater 2022;232:117938.
[3] Shahwaz M, Nath P, Sen I. A critical review on the microstructure and mechanical properties correlation of additively manufactured nickel-based superalloys. J Alloy Compd 2022;907:164530.
[4] Wu X, Makineni SK, Liebscher CH, Dehm G, Rezaei Mianroodi J, Shanthraj P, et al. Unveiling the Re effect in Ni-based single crystal superalloys. Nat Commun 2020; 11:389.
[5] He J, Cao L, Makineni SK, Gault B, Eggeler G. Effect of interface dislocations on mass flow during high temperature and low stress creep of single crystal Ni-base superalloys. Scr Mater 2021;191:23–8.
[6] Sharma A, Mondal C, Makineni SK, Chattopadhyay K, Banerjee D. Exploring the correlation between microscopic mechanisms and macroscopic behaviour in creep of a directionally solidified tungsten-free γ/γ′ CoNi-base superalloy. Acta Mater 2022;228:117738.
[7] Gu D, Zhang H, Dai D, Xia M, Hong C, Poprawe R. Laser additive manufacturing of nano-TiC reinforced Ni-based nanocomposites with tailored microstructure and performance. Compos Part B: Eng 2019;163:585–97.
[8] Coskun MB, Aksoy S, Aksit MF. Friction and wear characteristics of haynes 25, 188, and 214 superalloys against hastelloy X up to 540 °C. Tribol Lett 2012;45:497–503.
[9] Liu G, Du D, Wang K, Pu Z, Zhang D, Chang B. Microstructure and wear behavior of IC10 directionally solidified superalloy repaired by directed energy deposition. J Mater Sci Technol 2021;93:71–8.
[10] Yu Y, Zhou L, Cai Z, Luo S, Pan X, Zhou J, et al. Research on the mechanism of DD6 single crystal superalloy wear resistance improvement by femtosecond laser modification. Appl Surf Sci 2022;577:151691.
[11] Hou G, An Y, Zhao X, Zhou H, Chen J. Effect of alumina dispersion on oxidation behavior as well as friction and wear behavior of HVOF-sprayed CoCrAlYTaCSi coating at elevated temperature up to 1000°C. Acta Mater 2015;95:164–75.
[12] Lou M, Chang K, Xu K, Chen L, Lv J, Du Y, et al. Achieving exceptional wear resistance in cemented carbides using B2 intermetallic binders. Compos Part B: Eng 2023:249.
[13] Joseph J, Haghdadi N, Shamlaye K, Hodgson P, Barnett M, Fabijanic D. The sliding wear behaviour of CoCrFeMnNi and AlxCoCrFeNi high entropy alloys at elevated temperatures. Wear 2019;428–429:32–44.
[14] Liu X-B, Liu H-Q, Liu Y-F, He X-M, Sun C-F, Wang M-D, et al. Effects of temperature and normal load on tribological behavior of nickel-based high temperature self-lubricating wear-resistant composite coating. Compos Part B: Eng 2013;53:347–54.
[15] Sabahi Namini A, Dilawary SAA, Motallebzadeh A, Shahedi, Asl M. Effect of TiB2 addition on the elevated temperature tribological behavior of spark plasma sintered Ti matrix composite. Compos Part B: Eng 2019;172:271–80.
[16] Gong H, Yu C, Zhang L, Xie G, Guo D, Luo J. Intelligent lubricating materials: a review. Compos Part B: Eng 2020:202.
[17] Luo DW, Zhou Q, Ye WT, Ren Y, Greiner C, He YX, et al. Design and characterization of self-lubricating refractory high entropy alloy-based multilayered films. ACS Appl Mater Interfaces 2021;13:55712–25.
[18] Jia Q, He WH, Hua DP, Zhou Q, Du Y, Ren Y, et al. Effects of structure relaxation and surface oxidation on nanoscopic wear behaviors of metallic glass. Acta Mater 2022:232.
[19] Dreano A, Fouvry S, Sao-Joao S, Galipaud J, Guillonneau G. The formation of a cobalt-based glaze layer at high temperature: a layered structure. Wear 2019: 440–1.
[20] Stott FH, Lin DS, Wood GC. The structure and mechanism of formation of the `glaze' oxide layers produced on nickel-based alloys during wear at high temperatures. Corros Sci 1973;13:449–69.
[21] Kato H, Komai K. Tribofilm formation and mild wear by tribo-sintering of nanometer-sized oxide particles on rubbing steel surfaces. Wear 2007;262:36–41.
[22] Feng K, Shao T. Tribo-induced surface structure of Nickel-based superalloy at elevated temperature. Appl Surf Sci 2022:571.
[23] Bai L, Wan S, Yi G, Shan Y, Pham ST, Tieu AK, et al. Temperature-mediated tribological characteristics of 40CrNiMoA steel and Inconel 718 alloy during sliding against Si3N4 counterparts. Friction 2020;9:1175–97.
[24] Cheng Q, Zhang P, Ma X, Wan S, Jialin C, Hu W, et al. Microstructure evolution and wear mechanism of in situ prepared Ti–TiN cermet layers at high temperature. Compos Part B: Eng 2022:242.
[25] Liu C, Li Z, Lu W, Bao Y, Xia W, Wu X, et al. Reactive wear protection through strong and deformable oxide nanocomposite surfaces. Nat Commun 2021;12:5518.
[26] Chen X, Han Z, Li XY, Lu K. Lowering coefficient of friction in Cu alloys with stable gradient nanostructures. Sci Adv 2016;2:7.
[27] Chen X, Han Z, Li XY, Lu K. Friction of stable gradient nano-grained metals. Scr Mater 2020;185:82–7.
[28] Long JZ, Pan QS, Tao NR, Lu L. Abnormal grain coarsening in cyclically deformed gradient nanograined Cu. Scr Mater 2018;145:99–103.
[29] Cheng Z, Zhou H, Lu Q, Gao H, Lu L. Extra strengthening and work hardening in gradient nanotwinned metals. Science 2018;362:559–67.
[30] Duan FH, Lin Y, Pan J, Zhao L, Guo Q, Zhang D, et al. Ultrastrong nanotwinned pure nickel with extremely fine twin thickness. Sci Adv 2021;7:7.
[31] Hirth J, Lothe J. Theory of Dislocations. USA: John Wiley & Sons; 1982.
[32] Pan Q, Zhou H, Lu Q, Gao H, Lu L. Asymmetric cyclic response of tensile pre-deformed Cu with highly oriented nanoscale twins. Acta Mater 2019;175:477–86.
[33] Zhang Y, Niu T, Richter NA, Sun T, Li N, Wang H, et al. Tribological behaviors of nanotwinned Al alloys. Appl Surf Sci 2022:600.
[34] Xie XS, Chen GL, McHugh PJ, Tien JK. Including stacking fault energy into the resisting stress model for creep of particle strengthened alloys. Scr Metall 1982;16: 483–8.
[35] Kim IS, Choi BG, Hong HU, Yoo YS, Jo CY. Anomalous deformation behavior and twin formation of Ni-base superalloys at the intermediate temperatures. Mater Sci Eng, A 2011;528:7149–55.
[36] Sun W, Tan AW-Y, King DJY, Khun NW, Bhowmik A, Marinescu I, et al. Tribological behavior of cold sprayed Inconel 718 coatings at room and elevated temperatures. Surf Coat Technol 2020:385.
[37] Padmini BV, Mathapati M, Niranjan HB, Sampathkumaran P, Seetharamu S, Ramesh MR, et al. High temperature tribological studies of cold sprayed nickel based alloy on low carbon steels. Mater Today: Proc 2020;27:1951–8.
[38] Liu Z, Patzig C, Selle S, Höche T, Gumbsch P, Greiner C. Stages in the tribologically-induced oxidation of high-purity copper. Scr Mater 2018;153:114–7.
[39] Chen X, Ma Y, Yang Y, Meng A, Han ZX, Han Z, et al. Revealing tribo–oxidation mechanisms of the copper–WC system under high tribological loading. Scr Mater 2021:204.
[40] Rau JS, Balachandran S, Schneider R, Gumbsch P, Gault B, Greiner C. High diffusivity pathways govern massively enhanced oxidation during tribological sliding. Acta Mater 2021:221.
[41] Zhang HF, Yan HL, Yu H, Ji ZW, Hu QM, Jia N. The effect of Co and Cr substitutions for Ni on mechanical properties and plastic deformation mechanism of FeMnCoCrNi high entropy alloys. J Mater Sci Technol 2020;48:146–55.
[42] Dollmann A, Kauffmann A, Heilmaier M, Srinivasan Tirunilai A, Mantha LS, Kübel C, et al. Dislocation-mediated and twinning-induced plasticity of CoCrFeMnNi in varying tribological loading scenarios. J Mater Sci 2022;57: 17448–61.
[43] Warner DH, Curtin WA, Qu S. Rate dependence of crack-tip processes predicts twinning trends in f.c.c. metals. Nat Mater 2007;6:876–81.
[44] Haase C, Barrales-Mora LA, Roters F, Molodov DA, Gottstein G. Applying the texture analysis for optimizing thermomechanical treatment of high manganese twinning-induced plasticity steel. Acta Mater 2014;80:327–40.
[45] You ZS, Lu L, Lu K. Tensile behavior of columnar grained Cu with preferentially oriented nanoscale twins. Acta Mater 2011;59:6927–37.
[46] Freund LP, Messe O, Barnard JS, Goken M, Neumeier S, Rae CMF. Segregation assisted microtwinning during creep of a polycrystalline L1(2)-hardened Co-base superalloy. Acta Mater 2017;123:295–304.
[47] Zhu CZ, Zhang R, Cui CY, Zhou YZ, Qu JL, Gan B, et al. Effect of pre-strain treatment on mechanical properties of a Ni-Co base disk superalloy. J Alloy Compd 2022:905.
[48] Zhu W, Zhao C, Zhang Y, Kwok CT, Luan J, Jiao Z, et al. Achieving exceptional wear resistance in a compositionally complex alloy via tuning the interfacial structure and chemistry. Acta Mater 2020;188:697–710.
[49] Peczak P. A Monte Carlo study of influence of deformation temperature on dynamic recrystallization. Acta Met Mater 1995;43:1279–91.
[50] Momeni A. The physical interpretation of the activation energy for hot deformation of Ni and Ni–30Cu alloys. J Mater Res 2016;31:1077–84.
[51] Chen X, Schneider R, Gumbsch P, Greiner C. Microstructure evolution and deformation mechanisms during high rate and cryogenic sliding of copper. Acta Mater 2018;161:138–49.
[52] Huang JC, Gray GT. Microband formation in shock-loaded and quasi-statically deformed metals. Acta Met 1989;37:3335–47.
[53] Wang Z, Baker I, Cai Z, Chen S, Poplawsky JD, Guo W. The effect of interstitial carbon on the mechanical properties and dislocation substructure evolution in Fe40.4Ni11.3Mn34.8Al7.5Cr6 high entropy alloys. Acta Mater 2016;120. 228-39.
[54] Yin FX, Xia H, Feng JH, Cai MH, Zhang X, Wang GK, et al. Mechanical properties of an Fe-30Mn-4Si-2Al alloy after rolling at different temperatures ranging from 298 to 1073 K. Mater Sci Eng, A 2018;725:127–37.
[55] Feng K, Shao T. The evolution mechanism of tribo-oxide layer during high temperature dry sliding wear for nickel-based superalloy. Wear 2021:476.
[56] Inman IA, Datta S, Du HL, Burnell-Gray JS, Luo Q. Microscopy of glazed layers formed during high temperature sliding wear at 750 °C. Wear 2003;254:461–7.
[57] Lou M, Chen X, Xu K, Deng Z, Chen L, Lv J, et al. Temperature-induced wear transition in ceramic-metal composites. Acta Mater 2021:205.
[58] Geng Y, Chen W, Cheng J, Chen J, Zhu S, Yang J, et al. Selective solid solution tailoring mechanical and tribological synergy in heterogeneous single-phase high-entropy alloys at elevated temperatures. Tribol Int 2022:173.
[59] Zhou Z, Rainforth WM, Luo Q, Hovsepian PE, Ojeda JJ, Romero-Gonzalez ME. Wear and friction of TiAlN/VN coatings against Al2O3 in air at room and elevated temperatures. Acta Mater 2010;58:2912–25.
[60] Blau PJ. Elevated-temperature tribology of metallic materials. Tribol Int 2010;43: 1203–8.
[61] Sundaram NK, Guo Y, Chandrasekar S. Mesoscale folding, instability, and disruption of laminar flow in metal surfaces. Phys Rev Lett 2012;109:106001.
[62] Balachandran S, Zachariah Z, Fischer A, Mayweg D, Wimmer MA, Raabe D, et al. Atomic scale origin of metal ion release from hip implant taper junctions. Adv Sci 2020:7.
[63] Rynio C, Hattendorf H, Klöwer J, Eggeler G. On the physical nature of tribolayers and wear debris after sliding wear in a superalloy/steel tribosystem at 25 and 300°C. Wear 2014;317:26–38.
[64] Liang F, Xu X, Wang P, Zhang Y, Han Z, Chen X. Microstructural origin of high scratch resistance in a gradient nanograined 316L stainless steel. Scr Mater 2022; 220:114895.
[65] Fu H, Zhou X, Xue H, Li X, Lu K. Breaking the purity-stability dilemma in pure Cu with grain boundary relaxation. Mater Today 2022;55:66–73.

[66] Wu X, Yang M, Yuan F, Wu G, Wei Y, Huang X, et al. Heterogeneous lamella structure unites ultrafine-grain strength with coarse-grain ductility. Proc Natl Acad Sci USA 2015;112:14501–5.
[67] Zhu Y, Wu X. Heterostructured materials. Prog Mater Sci 2023:131.
[68] Molinari J-F, Aghababaei R, Brink T, Frérot L, Milanese E. Adhesive wear mechanisms uncovered by atomistic simulations. Friction 2018;6:245–59.